

Article

A Computer-Aided Algorithm Combined with an Integrated Downhole Method to Improve Shear Wave Detection and Damping Ratio Assessment: Theory and Preliminary Results

Gerardo Grelle 

Department of Civil, Constructional, and Environmental Engineering (DICEA), Sapienza University of Rome, Via Eudossiana 18, 00184 Rome, Italy; gerardo.grelle@uniroma1.it

Featured Application: The proposed computer-aided algorithm aims to introduce an approach to implement the performance and expand the capability of the downhole method in defining the shear wave velocity and the elastic damping ratio profiles.

Abstract: This contribution introduces a computerized semi-automated procedure coupled with a dedicated algorithm to improve shear wave velocity assessment and the on-site elastic damping ratio estimation of ground materials. The standard equipment of the downhole method is integrated with a horizontal geophone (guardian) placed on the field surface. Mask tapering and band multi-filter functions improve first arrival, recognizing and isolating SH-wave trains to estimate damping ratio profiles. These are computed by treating signals using a frequency–time combined approach (frequency–time packets method). The signals are corrected to consider the different source pulse amplitude, the effects of the propagation path, and scattering. The damping ratio profile is statistically computed in terms of the local drift of trend on the amplitude ratio series that would otherwise have a normal distribution centered on zero. These profiles intercept the lithology changes in the test sites and meet the damping values stemming from previous field tests and the laboratory experimental tests available in the literature regarding materials such as the ones investigated here.

Keywords: ground material damping ratio; downhole test; frequency–time signal analysis; seismic signals processing; shear wave



Citation: Grelle, G. A. Computer-Aided Algorithm Combined with an Integrated Downhole Method to Improve Shear Wave Detection and Damping Ratio Assessment: Theory and Preliminary Results. *Appl. Sci.* **2023**, *13*, 6080. <https://doi.org/10.3390/app13106080>

Academic Editor: Tiago Miranda

Received: 18 April 2023

Revised: 8 May 2023

Accepted: 12 May 2023

Published: 15 May 2023



Copyright: © 2023 by the author. Licensee MDPI, Basel, Switzerland. This article is an open access article distributed under the terms and conditions of the Creative Commons Attribution (CC BY) license (<https://creativecommons.org/licenses/by/4.0/>).

1. Introduction

The compressional P-wave and shear S-wave velocities, V_p and V_s , are fundamental parameters in the dynamic analysis and are significant in characterizing soils and rocks. V_s is considered a reliable parameter, more than V_p , for the definition of mechanical properties and behavior of soil materials. In various studies, V_s was taken into relation to cone penetration resistance [1–6], general geotechnical parameters [7–12], rock quality [13–15], liquefaction, and unsaturated soil densification [16–24] as well as, groundwater or hydrocarbon detection by combining V_s with V_p [25].

In an earthquake event, the propagation of seismic waves in cover deposits induces site effects which are physically modeled as complex damped-oscillator systems. These natural systems can change the amplitude and frequency of the input motion coming from the stiffer deep rock mainly about the shear wave velocity and damping ratio of ground materials composing the subsoil (e.g., [26–32]). Within this framework, the in-hole seismic methods provide more accurate and direct measurements of the body-wave velocities than the surface seismic methods. However, these latter, although less accurate, are often used in engineering practices based on simplified or empirical computational models (such as those based on V_{s30} or equivalent V_s referred to the bedrock) because they are cheaper than in-hole methods. Surface methods are favored by their good performances in sites with

low-complexity geology [33]. These advantages increase with natural and anthropic effects that often affect or eclipse the first arrivals in the in-hole methods to different degrees.

Some natural parameters, such as the ground dynamic ones, are frequently difficult to detect and measure just using direct observation because these parameters are affected by aleatory behaviors or comprising phenomena resulting from combined multi-effects. Therefore, measurement of these parameters needs on-site sampling and laboratory control tests. However, the sampling may produce the decontextualization of tests from the natural site, although these are highly accurate in measurement.

The present work aims to increase the downhole performance on this aforesaid issue by introducing a new computerized algorithm. This one, associated with standard down-hole equipment integration, tries to give more reliability and efficacy to the DH method in its standard setting. The proposed algorithm improves the recognition of the first arrivals of SH waves, but mainly here it introduces a novel processing data method to compute profiles of the material elastic damping ratio. This is based on filtering and correction of signals to isolate them from distance attenuation and multi-layer scattering effects; finally, a probabilistic data drift model returns the vertical damping profile.

2. Background

2.1. In-Hole Seismic Surveys

Crosshole and downhole methods are standard and consolidated tests introduced for accurate detection of the V_s profiles and other dynamic parameters of soils under natural conditions. The seismic crosshole method (ASTM D4428/D4428M) requires two, or better three, holes and the knowledge of their vertical deviation by clinometer measurements. SV waves are progressively generated with a proper hammer in one of the holes and recorded in the other ones. Considering the real propagation line path, ambiguities occur when soft materials constitute thinner layers among hard material layers. Such ambiguities are partially overcome by using additional tomographic inversion processing [34,35]. The short distance, between the source and gauges suggests this method to define the elastic material damping values. Crosshole surveys are complex and very expensive tests. Conversely, downhole surveys are easier and cheaper, so these are preferred and frequently used in engineering practices when advanced dynamic analyses are required.

The downhole seismic test (ASTM D7400/D7400M) consists of in-single-hole records of P-waves and polarized SH waves both produced by ground surface sources located near the hole. Seismic data are recorded at multiple progressive vertical steps, associated with multiple hammer shots, or rarely with the vertical geophonic array. Polarized SH waves develop from left and right shots against the side faces of a wood/metal block pressed to the ground surface. Instead, P-waves develop from vertical shots against a strike plate. The hammer is equipped with a start-record device, and each recorded step is performed by capturing the waves with a triaxial geophonic package in the hole. The package consists of two orthogonal horizontal geophones and a vertical one. The short horizontal distance between the source and the 3D package minimizes the influence of the curved travel path due to refraction within the layered subsoil. This assumption defines a simplified model based on linear and direct wave propagation with the verticalization of the seismic ray along the depth. Although this simplification is being used in travel-time processing, it cannot be used in measuring attenuation/damping.

2.2. Factors Affecting Shear Wave Arrivals

Many factors influence the downhole signal quality. These factors are reflected in unclear detection (or ambiguity) of the classic break shape associated with the first arrivals of SH waves (picking). In addition, layered, inhomogeneous, and anisotropic materials promote scattering by refraction that overlaps the geometrical attenuation and damping. Good signals primarily depend on the quality of the borehole conditioning, the procedures used to make it, the source device type (aleatory pulse or monochromatic signals), and the acquisition system. These procedures, explained in detail in ASTM D7400/D7400M, are

also used to contain the disturbance effects. However, local logistic difficulties sometimes require additional actions or modifications from the standard. Specifically, the instability of the sidewall during the drilling phase requires the use of a metal casing, which must be progressively pulled out when the fluid grout mixture is injected into the interspace at the end of the borehole. This ensures the progressive expelling of water by the borehole's head when it is present. Furthermore, sources should not be placed on road surfaces/paving or other stiff surfaces. Otherwise, it is necessary to prevent direct links between these surfaces and the pipe head by not cementing the interspace at the near-surface trunk. In addition, to limit the changing polarity in signal capturing, the constant alignment in borehole horizontal sensors with the plank (source) has to be assured; this is fundamental in the damping estimation even more. Likewise, an adequate clamping pressure ensures the transmission of the wave, and a constant contact pressure excludes additional attenuation anomalies when a damping estimation analysis is tried.

Shear waves stemming from the surface source generally suffer from interferences by wave trains with different natures, even when ASTM standard procedures are strongly observed. Therefore, direct SH waves are mixed or are preceded in some cases, with reflected/refracted waves coming from scattering anomalies. Polarized waves generated by other sloped surfaces could mix too [36,37]. The effect of these waves on first arrivals is unconsidered by the 1D-numerical inversion model because usually assumes a flat layering of simplified subsoil. Tube waves and noise can add more relevant disturbance yet. The tube waves propagate with a rotational path around the tube surface. This effect seems more persistent when the tube is dry [37,38]. Instead, when the casing is filled with water, a pressure pulse is generated by the impact of SH waves and propagates along the tube [37,38]. Therefore, in either case, the tube waves take the same polarity as the promoting shear waves and keep it during propagation. Additionally, compressional waves in tube fluid attenuate less rapidly than the body waves, so their disturbance effect increases with the depth.

2.3. Damping Ratio

The damping phenomenon is by energy dissipation during the wave propagation in the medium. Most experts define the damping ratio as the energy loss in a close hysteresis loop. The latter is obtained in laboratory tests by applying frequency-modulated harmonic shear loads/unloads and measuring the stress vs. strain values [39–41]. Another laboratory technique is based on counting the free vibrations after forced cyclic loading. Therefore, the laboratory techniques lead to the accurate measuring of the damping ratio at different strain levels. However, these tests suffer some disadvantages despite their good accuracy. Mainly, coarse granular soils, mixed debris soils, and stony layers are very difficult to test samples of large dimensions. In addition, many tests perform on saturated samples, while the unsaturated (in suction) ones are the minor part. Finally, the estimation of damping profiles requires frequent sampling along the drilling, entailing long, time-consuming, and highly expensive tasks.

In in-hole seismic methods, the low shear-strain level induced by pulse waves leads initial linear damping ratio value that is also the minimum one. Therefore, the low contribution in attenuation, due to the linear material damping, is very difficult to detect using the common in-hole seismic methods. The difficulty increases when aleatory signals generated by simple hammering are used combined with propagation in inhomogeneous materials. However, this hard challenge was approached by several authors using different methods [42–44]. All these methods include the use of the shear beam equipment, which permits frequency/amplitude control of the signals at the source to exclude the aleatory component associated with the hammer shots. The time-domain method, proposed by Mok et al. [45] on crosshole data, relies on measuring the SH-wave amplitude delta at two different depth steps. The two signals are cleaned by the chopper and tapering techniques. Thus, the signals have correct form linear geometric propagation and scattered interface transmission effects, and the solution of the hyperbolic decay outputs the damping ratio.

The difficulty in applying this method is to define the real multi-refraction propagation and therefore the incident wave and its scattered transmission effect. The unidimensional numerical method, used on a linear viscoelastic model, solves the problem through the best fit of numerical and experimental signals. However, the main limits of this model are due to considering the vertical incident waves and being very time-consuming in step-by-step computations. According to Stewart and Campanella [44], the spectral slope method is the most promising one. Based on spectral domain analysis, the method seems to give the best performance by using sources producing mono-frequency signals [42–44]. The spectral slope considered by the method solves the problem of the geometrical attenuation but not the amplitude change due to the scattering. In this regard, the method shows good performance when large vertical stretches of uniform material are measured. Moreover, the spectral ratios usually have a not linear trend in the frequency interval covered by the SH-wave train. Thus, the subsequent linearization introduces a high subjectivity in the outputs (e.g., as is shown and discussed in Section 6).

The knowledge of low-strain damping values is relevant in linear dynamic analyses. In addition, it substantially contributes to the empirical definition of the stress–strain curves used in the non-linear analysis. In fact, with the increase in the number of laboratory tests, regression laws about shear modulus and damping ratio degradation curves increase. It seems that these have a good relationship with the material properties and confining pressure. The regression laws formulated so far require the initial damping ratio, D_{min} (at low strain), e.g., in the Masing model [46] and other authors [47–51]. Instead, Taboada et al. [52] show that D_{min} has a weak relation with the confining stress but a greater affinity with $D_{max} - D_{min}$ through numerous sandy soil tests.

3. System and Test Sites

The proposed approach requires specific low-cost tools to integrate the standard in-field instrumentation and an appropriate configuration supports the novel processing of signals. Regarding the test-setting and the ray path model linked to equipment configuration, Figure 1 reports a synthetic conceptual framework of the system. Instead, Table 1 reports all variables and mathematical functions considered in the theoretical treatment of the proposed method.

Table 1. Symbology of the variables present in this work.

Symbol	Description	Symbol	Description
$A(t)$	Wave amplitude	λ	Wavelength
A_0	Initial (maximum) wave amplitude	l_i	Wave down-propagation line
α_F	Angle of reflected wave	ρ_i	Density of the i th-layer
α_I	Angle of incident wave	σ_m	Average slowness of the SH-waves
α_R	Angle of refracted wave	S	Transmitted scattering coefficient
$\Phi(f_c, \Delta f)$	Filter passband function centered on f_c	T	Period
Δf	Frequency interval	t	Time
$D(\gamma)$	Shear-strain depending damping	t_0	Delay time
dl_i	Wave down-propagation stretch	t_c	Corrected travel time to vertical distances
dt	Time step (travel time in a given dz -step)	t_x	Clear time of the first arrival
dz	Vertical measurement step	T	Period
f	Frequency	V_P	Compressional wave velocity
f_c	Central frequency	V_S	Shear wave velocity
f_H	Upper cut-off frequency	$w(t)$	Mask tapering function
f_L	Lower cut-off frequency	ω_n, ω	Natural angular frequency
dt	Sampling time in recording	$X(t)$	Signal recorded on x direction
FFT	Fast Fourier transform	$Y(t)$	Signal recorded on y direction
h	Distance between the source and borehole	$Z(t)$	Signal recorded on z direction
ξ, D_{min}	Initial linear damping	z_i	Depth at the i th-step
φ	Angle of direct wave by source	Ω	Computational loop
k	Wavenumber	FFT	Fast Fourier transform

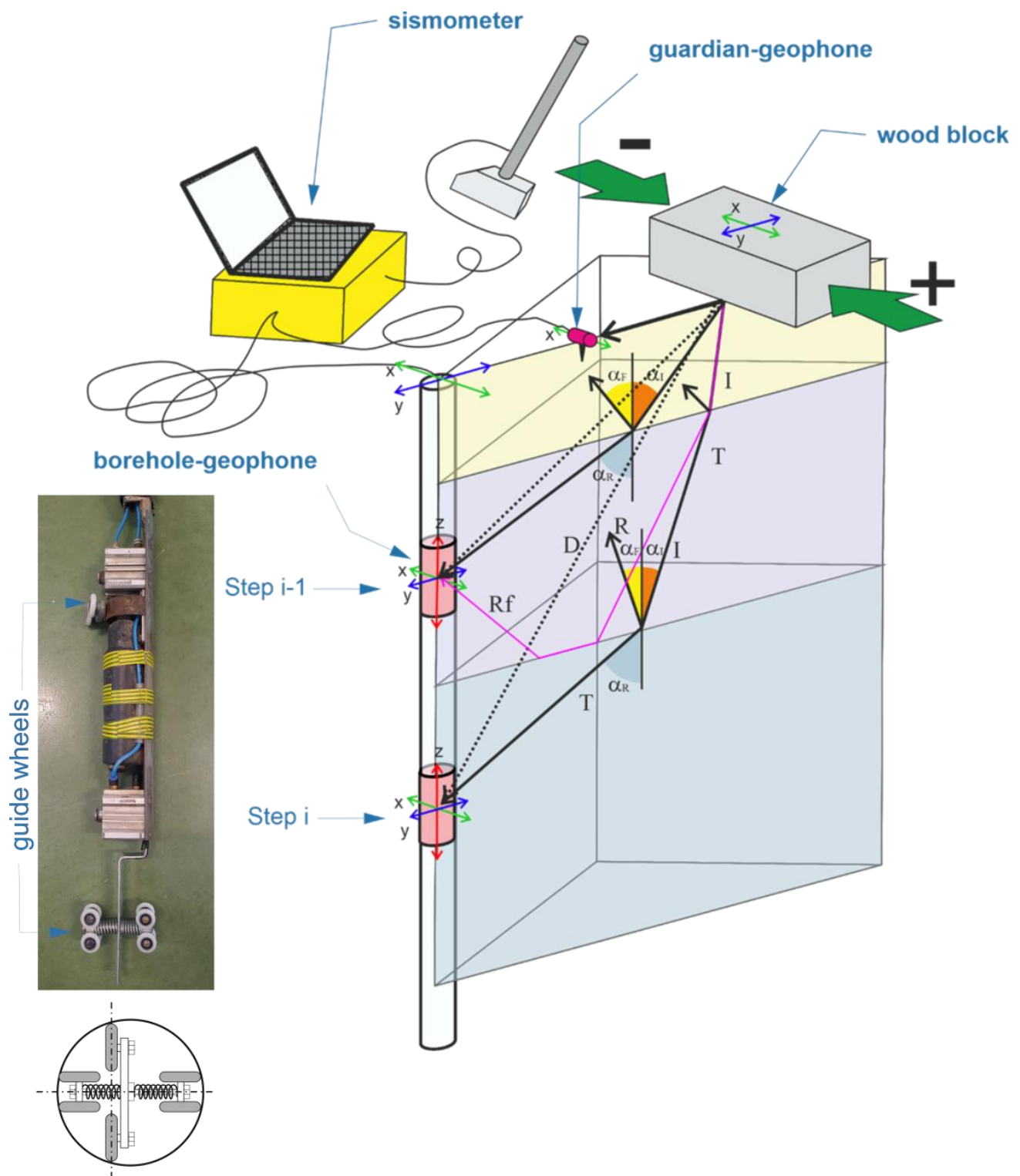


Figure 1. Downhole setup and wavefront ray path: I = incident wave; T = transmitted (refracted) wave; R = reflected wave; D = theoretical simplified directed wave. Detail of borehole geophone with pneumatic clamping.

The equipment configuration used in the field is the basic standard one (ASTM D7400/D7400M) with additional devices. Therefore, this configuration consists of the three-axis geophonic package and a plate for vertical impact to get P-waves. Instead, a wood block constrained to the ground produces SH waves when the hammer horizontally hits it. The configuration completes by an additional horizontal geophone on the field surface, which acquires the signals in sync with the three-axis geophone in the hole. The un-sync discrepancy is checked during acquirement by the guardian geophone and following corrected by elaboration, while the system limits the influence of the interference waves during processing by introducing tapering functions. Although ASTM does not contemplate the surface geophone, this is rarely used to check the correctness of the start times. This geophone, here named “guardian geophone”, takes the main role here because it includes additional functions to reach the goals of the proposed method. Geophones with a characteristic frequency of 4.5 Hz, while a sample time of 0.064×10^{-3} s and a 24-bit seismograph were used in the case studies.

The 3D geophonic package is equipped with an ancillary device to prevent or minimize the rotation during vertical running. The device, one of a kind, uses push-to-friction and conservation of angular moment to contrast the rotation. A coupled wheels orthogonal guide system stabilizes the rotation system and maintains unchanging the rotation axes of the wheels during down and upward. The system’s rotational axis does not match the center of the borehole contrasting with the rotation of the 3D packet (detail in Figure 1).

Two boreholes, b1 and b2, are the test sites (Figure 2). These have respective depths of 48 m and 40 m and are located in Rieti, a city in central Italy. This area was recently involved in the 2016–2017 earthquake sequence (M 6.0–6.5). The boreholes are in seismic and geotechnical surveys plan of the seismic securing design of school buildings. The Rieti urban area falls in an Apennines endorheic plain characterized by recent complex geology consisting of alluvial and carbonate precipitation deposits set in mixed cyclic sequences. This geological frame evolves consistent and frequent scattering phenomena producing waves that mask the direct SH ones. Data from b1 describes each step of the procedure, but the results are reported for both.

A prototype Python computer code was developed, and it is composed of three computational modules. The modules are aimed at (i) picking and optimizing the extraction process of the SH-waves; (ii) V_p and V_s profiles; (iii) the material damping ratio profile.

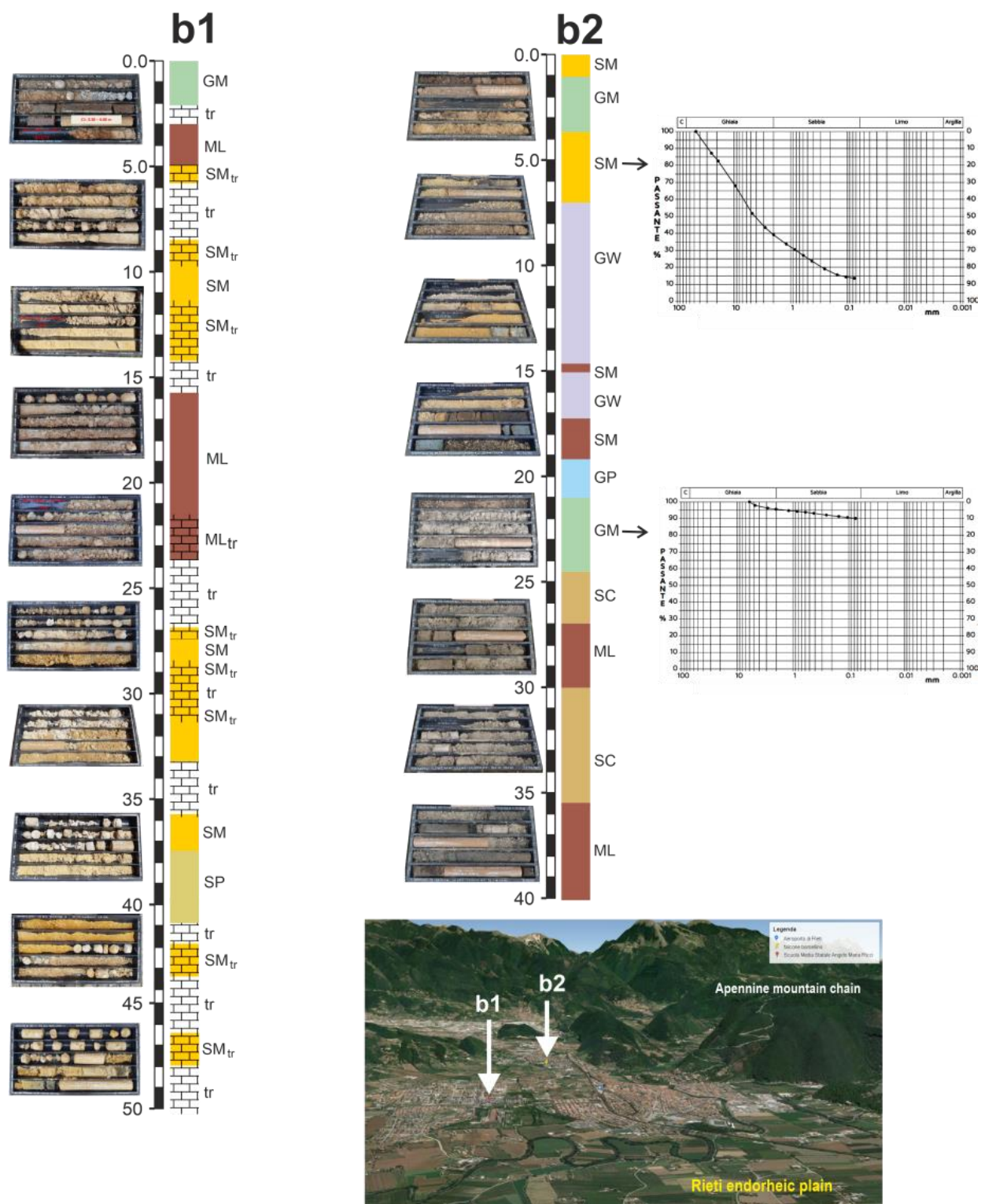


Figure 2. Borehole stratigraphic logs and site surveys framework: b1, located at the “Angelo Mattia Ricci” school (lat. 42.413650; lon. 12.857292); b2, located at the “Falcone Borsellino” school (lat. 42.409310; lon. 12.878351). The lithologies are defined using the international particle size classification of USGS. GM—gravel mixed with sand and silt; ML—silt and clay; SL—silty sand; SP—clean sand; SM_{tr}—soft travertine or sandy travertine; tr—hard travertine. Particle size distributions are from original reports.

4. Shear Wave Velocity: Method and Computational Steps

4.1. SH-Waves by Optimized Bring-Out Process

Signal processing tools, such as shift start time, amplitude equalization, and passband filters, are in this computational step. Pass-band filter ranges are differentiated for vertical and horizontal wave components by assuming values of 10 and 100 Hz for SH-waves and 20 and 200 Hz for P-waves. These functions are joined with the main masking-magnification function for SH-wave detection. At the guardian geophone, signals from the hammer impact source show different amplitudes but a clear and invariant predominant frequency (Figure 3a). This invariance admits to using this kind of source in damping assessment.

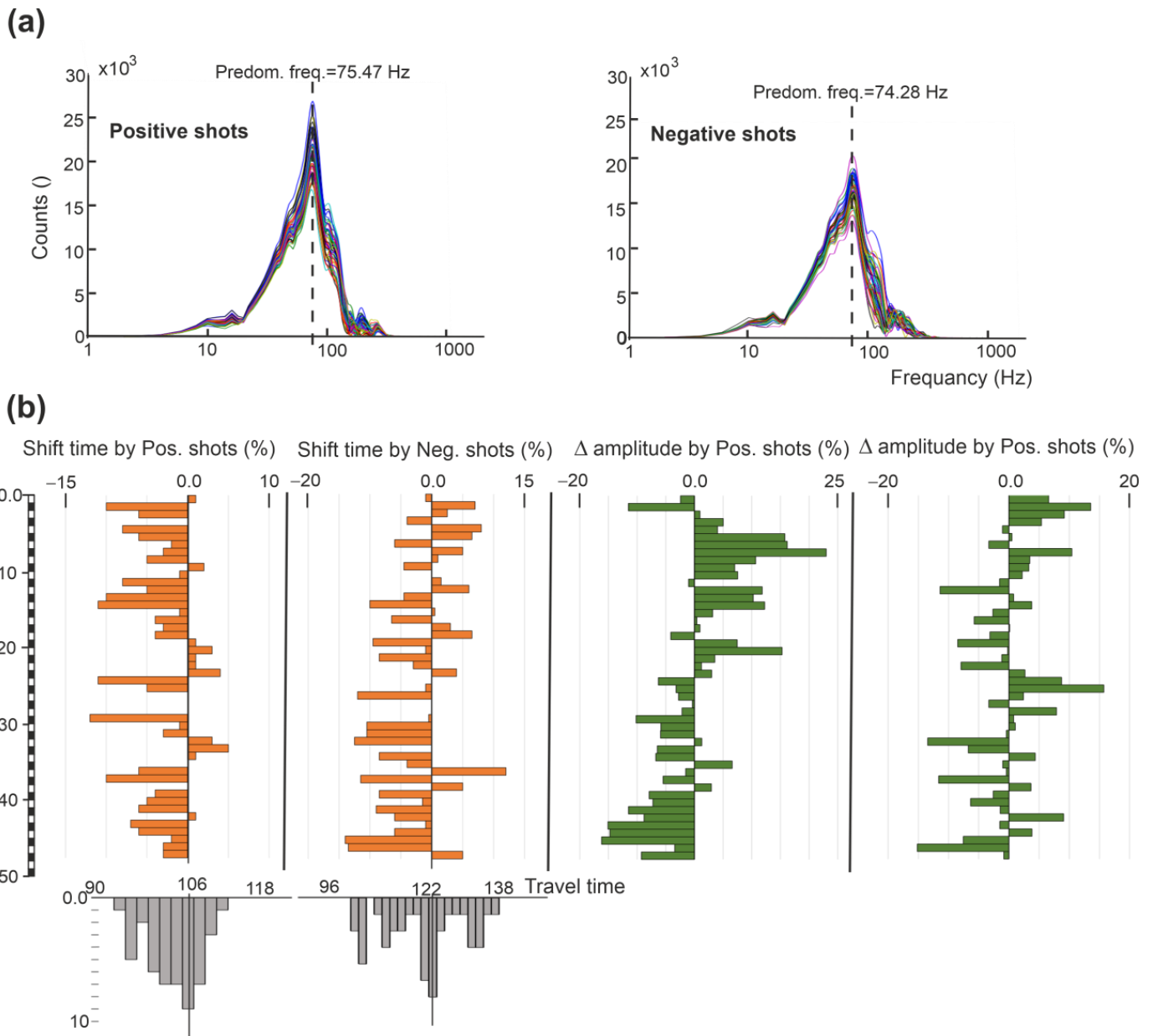


Figure 3. Guardian geophone signal analysis for correction: (a) FFT of positive and negative shots showing high central frequency predominance; (b) shift time (orange) and amplitude change (green). Travel time distribution and modal values (grey diagrams) are reported in terms of time-sampling numbers (the simple time is 0.064×10^{-3} s).

The correction of the starting time (Figure 3b) is by considering the first arrivals at the guardian geophone because all waves theoretically arrive at the same time on it. Consequently, it is possible to identify the lag times when this simultaneously does not appear in the practice. Positive or negative time shifts are identified by comparing each travel with the modal value of the complete series detected at the guardian geophone. For “late start cases”, the corresponding signal detected at the 3D geophonic package is corrected by joining zero elements at the head and by cutting off the end of the same number of elements. The reverse manner is for “early start cases”. The number of zero elements depends on the time shifts detected at the guardian geophone. Automatically, travel times at the guardian geophone are detected by associating them with the times given by the crossing of an assigned amplitude value. This has to be set higher than the noise (2% of the maximum in this study).

The mask function is a double exponential tapering function that zeros the signal before and after a target interval containing the first arrival of the S waves. The time shifting of the target interval runs linearly on the signal series. However, this interval is sufficiently large to intercept hard rollover and nonlinear trends of first arrivals, even when these are associated with deep borehole series (Figure 4). The linear trend (in Equation (2)) is defined by assuming: (i) a clear travel time t_x within the signal series and (ii) initial delay time, t_0 . The travel time has preferably to select a signal among the deeper ones, that clearly shows the first arrival of the SH waves, while t_0 is defined under or on the first arrival of the first couple of signals that should be the clearest one. The equations composing this function at a generic i -th depth are the following:

$$w(t)_i = \frac{\vartheta(1 - \vartheta)}{\max[\vartheta(1 - \vartheta)]}, \quad (1)$$

$$\text{where } \vartheta = e^{[1 - (t_0 + (\sigma_m idz)/t)^2]} \text{ and } \sigma_m = \frac{t_x - t_0}{z_i}, \quad (2)$$

σ_m is defined as mean slowness, while the mask function $w(t)_i$ takes values in the interval from 0 to 1. Thus, it follows that the new i -th signal is computed as follows:

$$A(t)_{i_{msk}} = A(t)_i w(t)_i, \quad (3)$$

The performance obtained by using the mask function (Figure 4) shows that the progressive zeroing under target interval weakens the overlapping effect produced by waves of different natures, strenghtening the direct SH ones, while zeroing above weakens, up to nullification, the presence of multi-reflected/refracted waves.

4.2. Velocity Profiles

This module computes V_p and V_s profiles using the interval time and slope-break technique (Figure 5) based on picking or multi-picking values from each measured step. Multi-picking consists of a picking set of the same signal (or coupled signals) which is defined by collecting all uncertain arrivals (picks) within a short time-lapse containing, hypothetically, the correct one. Multi-picking values derive both from natural and treated masking tracks. Subsequently, univocal first arrivals are computed as median values of all picking values detect in each vertical step. In the slope-break technique, velocity layers are priority defined according to the rollovers of SH-wave arrival trends, and the depths intercepted are to define V_p values later.

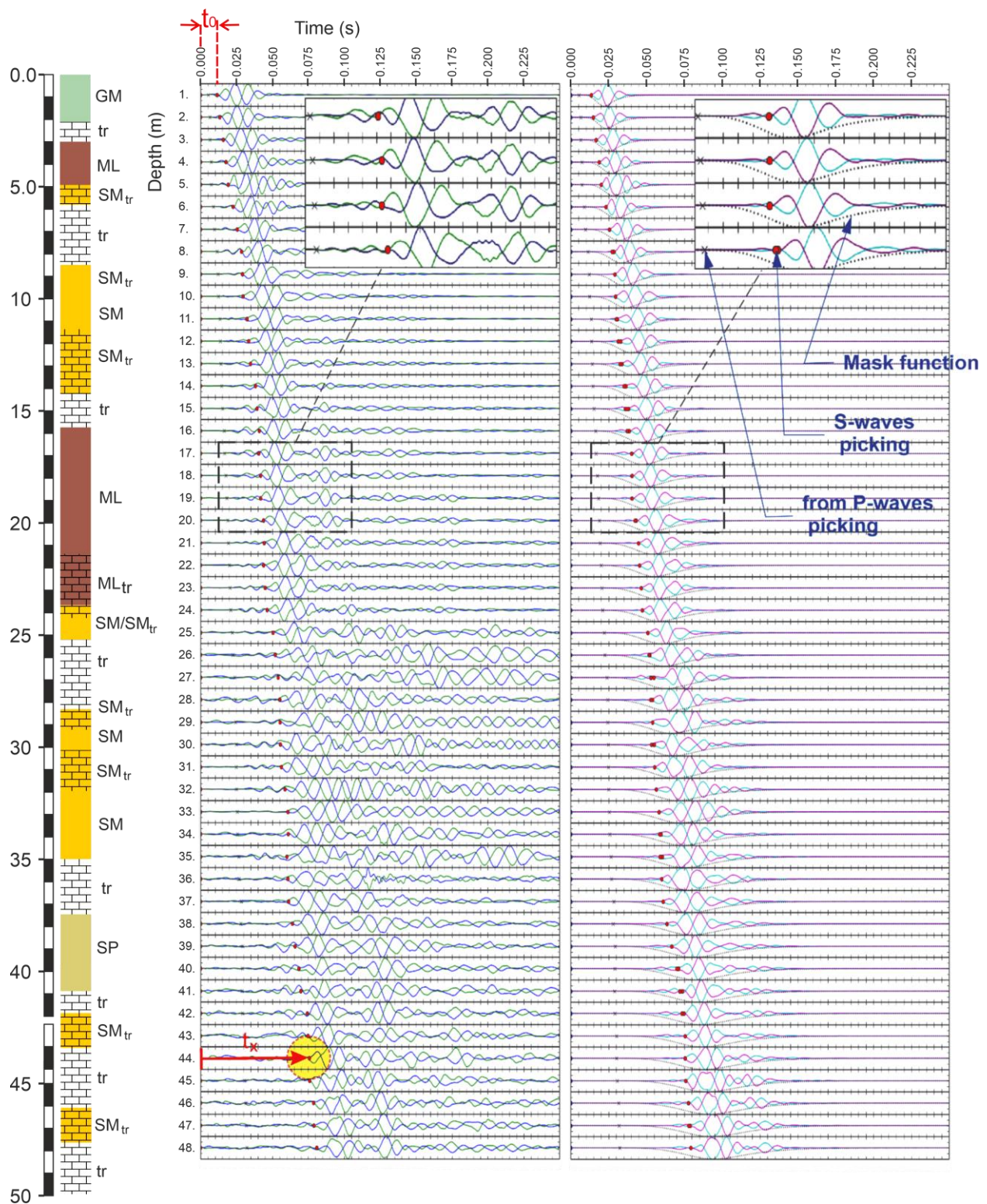


Figure 4. Picking on signals without (left) and with the masking function (right).

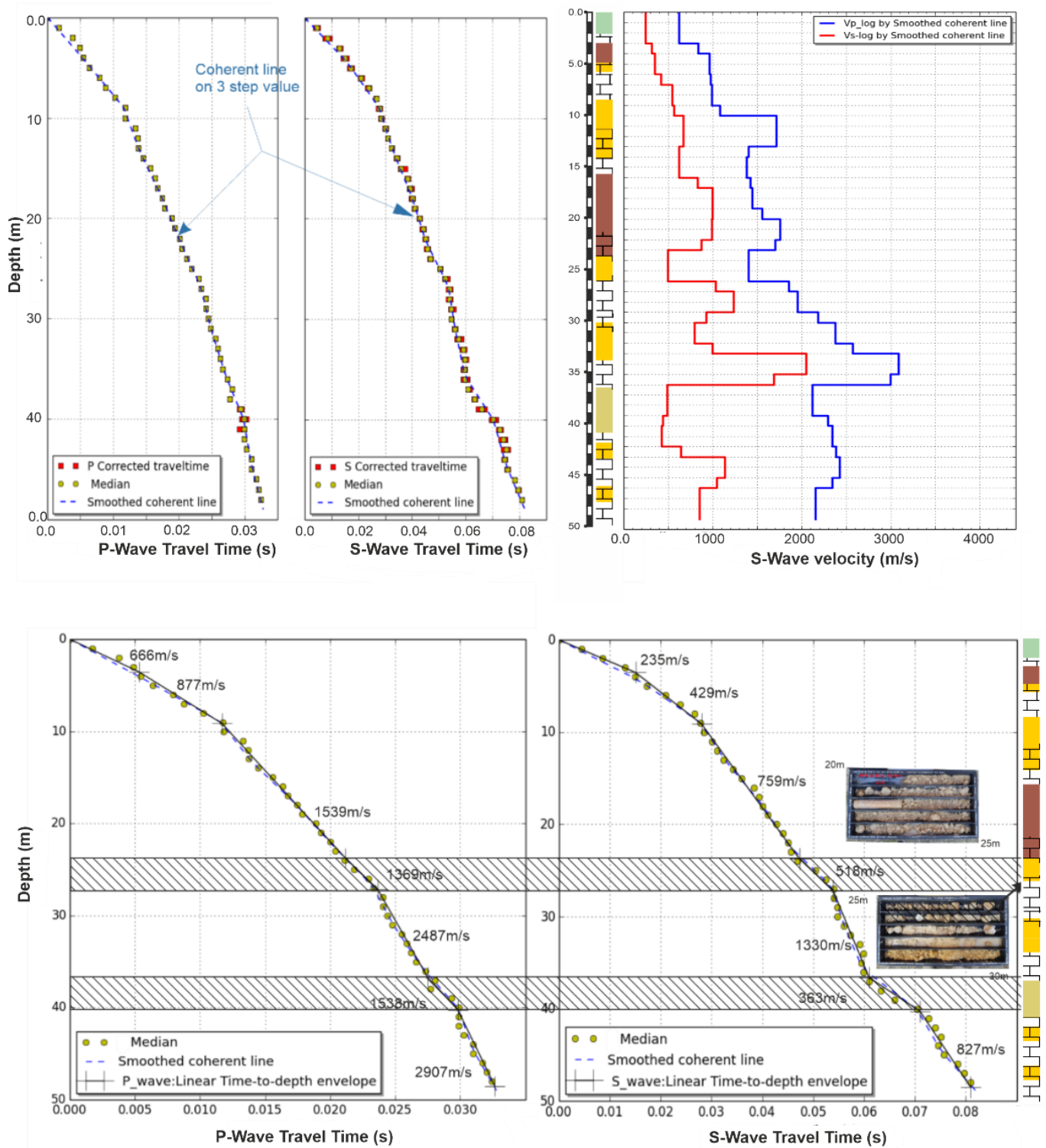


Figure 5. Corrected travel-times curves of P-waves and SH-waves picking fitted by smoothed coherent line by using interpolation on three time-steps to return interval velocity profiles (graphs above); V_p and V_s are defined by manual break slope technique (graphs below).

A smoothed line fits the arrivals stemming from the median values of the corrected travel times. These are defined by the direct linear source-geophones travel model observing ASTM D7400/D7400M as follows:

$$t_{ci} = t_i \cos \left[\tan^{-1} \left(\frac{h}{z_i} \right) \right], \quad (4)$$

The smoothing degree is assumed by taking into account the break-slope recurrences along the arrivals distribution trend. Thus, a number of arrivals define the light of tracts subject to linear interpolation by controlling the flexibility of the smoothed line (Figure 6). This flexibility defines the vertical resolution of the velocity profiles hence. High flexibility of the smoothed line may induce local incoherence of velocity due to single V_s and V_p outliers. In contrast, low flexibility simplifies the velocity profiles occulting eventual slim layer presences.

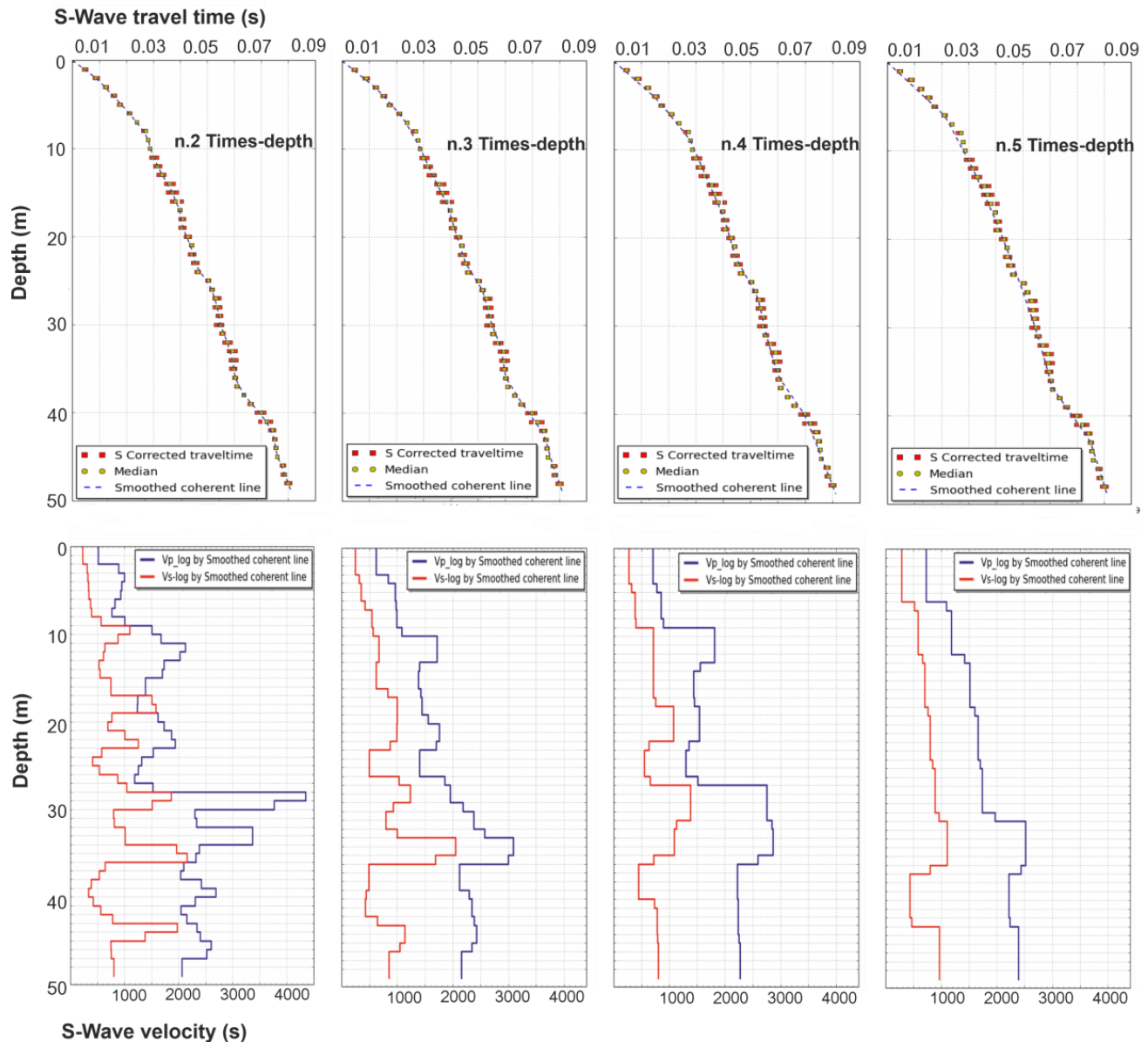


Figure 6. Coherent smoothed line interpolation and relative interval velocity profiles.

5. Damping Ratio: Method and Computational Steps

The method has developed from theoretical bases driving the damped harmonic signal propagation in the time domain (Figure 7). The exponential decreasing of the signal modulus is investigated in two generic consecutive depth steps, z_i and z_{i+1} , with reciprocal distance, dl , associated with a differential travel time, dt . In this interval, considering the material as uniform and homogeneous, the amplitude of the signal changes as follows:

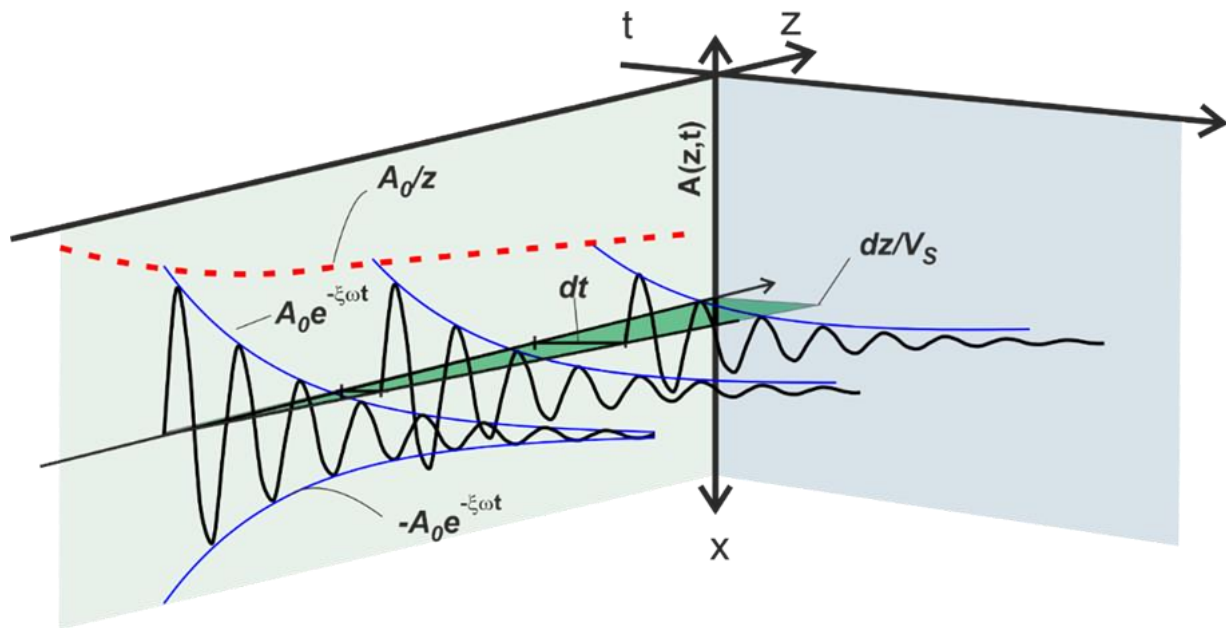


Figure 7. The theoretical combined effect of geometrical attenuation and damping material ratio in discrete progressive depth steps.

$$A_{z_i}(t) = A_0^{-\xi \omega t} \cos(\omega t + \rho), \quad (5)$$

$$A_{z_{i+1}}(t) = A_0^{-\xi \omega(t+dt)} \cos(\omega t + \rho), \quad (6)$$

At the maximum amplitude is in $t = 0$, where

$$\frac{A_{z_i}}{A_{z_{i+1}}} = \xi \omega dt, \quad (7)$$

from which

$$\xi = \frac{\ln\left(\frac{A_{z_i}}{A_{z_{i+1}}}\right)}{\omega dt}, \quad (8)$$

considering also that $\omega = 2\pi f$, and $dt = dl/V_s$, it results that

$$\xi = \frac{\ln\left(\frac{A_{z_i}}{A_{z_{i+1}}}\right) V_s}{2\pi f dl}, \quad (9)$$

The amplitude ratio is from wave-packets, consisting of modified SH wave trains, regarding signals crossing two consecutive depth steps. The $n\pi$ -packets stem from signals coming from different narrow passband filters and cutting by a mask tapering exponential function then. In this way, it is possible to assume that an $n\pi$ -packet consists of monochromatic signals with lengths multiples of $k(T/2)$, where k is the wavenumber (details on the development of $n\pi$ -packets are reported in Section 5.1). For these signals, the ratio between the maximum amplitudes is equal to the ratio between absolute averages. This assumption solves the amplitude ratio in Equation (9), and its general mathematical formalism is as follows:

$$\frac{A_{z_i}}{A_{z_{i+1}}} = \frac{\int_t^{t+k\frac{T}{2}} |A_{z_0}^{-\xi \omega t} \cos(\omega t + \rho)| dt}{\int_{t+dt}^{t+dt+k\frac{T}{2}} |A_{z_0}^{-\xi \omega(t+dt)} \cos(\omega t + \rho)| dt} = \frac{|A_{z_i}(t)|_0^{k\frac{T}{2}}}{|A_{z_{i+1}}(t)|_0^{k\frac{T}{2}}}; k \in n > 0, \quad (10)$$

To isolate the damping effect from other ones, the signals in Equation (10) need pre-processing. This is to minimize the natural scattering and geometrical attenuation effects, such as epistemic/noise ones, that contribute to modifying the amplitude of signals on par (or more) with the damping effect.

5.1. Scaling to Equalize the Source Effect

The mask tapering function $w(t)$ isolates the direct SH waves:

$$A_2(z_i, t) = A_1(z_i, t)w(t)_i, \quad (11)$$

Unlike in the previous computational module, this function applies to natural signals by sampling the signal starting from picking time, while the length assumed for composing the wave packets (details at point 5.4) defines end-time.

5.2. Seismic Ray Path

In this computational module, the path of the seismic ray computes considering the ray deviation due to the refraction. The subsoil model assumed in the computation is a regular dummy n-layered subsoil with equidistant layers with a thickness equal to the distance step dz . Therefore, considering the Snell law, the wave running through the i th-layer is:

$$dl_i = dz \cos \alpha_{R_i} = dz \cos \left[\sin^{-1} \left(\frac{\sin \alpha_{I_{(i-1)}} V_{S_i}}{V_{S_{(i-1)}}} \right) \right], \quad (12)$$

The term in the brackets is the refracted angle α_{R_i} , which correspond to the incident angle $\alpha_{I_{(i+1)}}$ in the subsequent layer, while the first incident angle is

$$\alpha_{I_1} = \tan^{-1} \left(\frac{dz}{h} \right), \quad (13)$$

In (12), when the shear wave velocity does not change, the result remains unvaried, implying that a linear propagation in uniform material occurs in the two consecutive measure steps.

5.3. Amplification and De-Amplification by Scattering

The SH-wave amplitude modification due to the scattering phenomenon was discussed by [42] by introducing reflection and transmission scaling coefficients. These depend on the density and shear velocity of the two media and the incident angle; specifically, the transmitted scattering coefficient is defined as:

$$S_i = \frac{2\rho_{(i-1)} V_{S_{(i-1)}}^2 q_{(i-1)}}{\rho_{(i-1)} V_{S_{(i-1)}}^2 q_{(i-1)} + \rho_i V_{S_i}^2 q_i}, \quad (14)$$

where generic q_i is described as

$$q_i = \frac{1}{V_{S_i}} \sqrt{1 - (V_{S_i} p_{I_i})^2}, \quad (15)$$

p_{I_i} is defined as the slowness along the interfaces and depends on incident angle as follows:

$$p_{I_i} = \frac{\sin \alpha_{I_{(i+1)}}}{V_{S_i}}, \quad (16)$$

In the (16) density is empirically estimated [53,54] as

$$\rho = 4.4 V_S^{0.25}, \quad (17)$$

It is noteworthy that in (15), when the shear wave velocity does not change in two consecutive measures steps, the transmitted coefficient is equal to one, as expected from propagation in the uniform material.

5.4. Wave Packets Development

The SH-wave packets develop by using passband filtering, $\Phi(f_c, \Delta f)$ and tapering cut functions on the signals stemming from Equation (12). Therefore, the signals composing these packets are characterized by short frequency intervals and lengths modulated by low and different wavenumbers. The filter intervals are defined by the progressive enlargement of limits since an average central frequency, f_c ; this value is obtained from the spectral maximum value of the signal detected at the guardian geophone and extracted from the Konno and Ohmachi smoothing FFT spectrum [55]. Figure 8 shows the combination scheme between the PB-filter and the tapering cuts. Specifically, a given number of n progressively expanded passband intervals are subsequently combined with the tapering cut functions to obtain signals with an assigned wavenumber, k . The starting points of the tapering cut are the picking times, while the final times are defined by values of frequency, f_c , and the assigned wavenumbers. To prevent different smoothing at the ends of each SH-wave packet, a common representation in the virtual time axis, from 0 to 1, was obtained by resampling the signals with different dt after PB-filtering and before applying the mask tapering function. In this manner, the results from tapering cut function are independent of absolute time defined by f_c and k values. Thus, all signals result in (i) tapering in the same manner, (ii) starting from the picking time, and (iii) stretching out to $k(T/2)$. Generally, k values ranging from 1 to 5 capture a substantial part of SH waves. The generalized Function (18) satisfies the previously explained combination to develop sets of quasi-monochromatic signals for each i th-depth step:

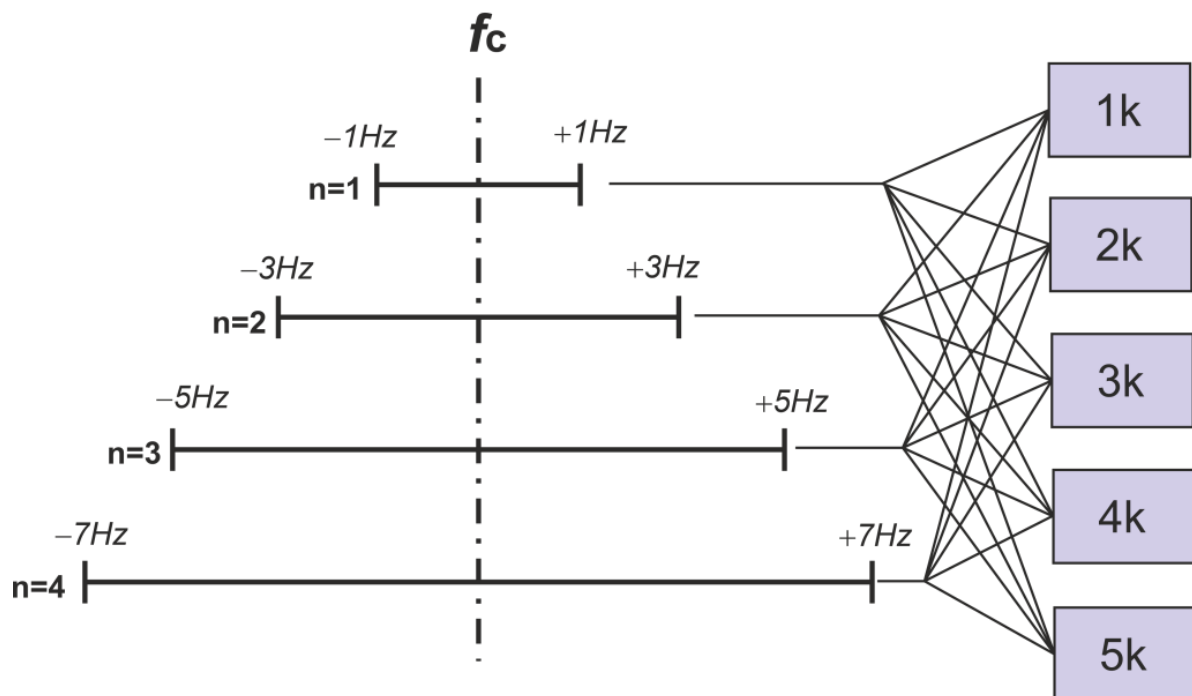


Figure 8. Combination between passband filter operation and wavenumber composing the signals.

$$A_2(z_i, t) \rightarrow \Omega\{A_2[z_i, k, \Phi(f_c \pm \Delta f_n)]\}_{n \in [1 \div 4]; k \in [1 \div 5]}, \quad (18)$$

The results report as $A^*(z_{i-1})$ and $A^*(z_i)$ to solving the Equation (19) for two consecutive depth steps.

5.5. Damping Ratio Computation

The damping ratio obtained from packets of quasi-monochromatic signals needs correction of geometrical attenuation and scattering effects (Figure 9). In this regard, the amplitude ratio of Equation (10) resolves by considering the natural hyperbolic attenuation of the body waves, with $1/z$ law (Equation (12)), and including the scattering coefficient of the transmitted wave (Equation (14) in a reversed way. Thus, combining the aforementioned equations and considering uniform material between two consecutive z_{i-1} and z_i ($i > 1$) measurements, the damping ratio is as follows:

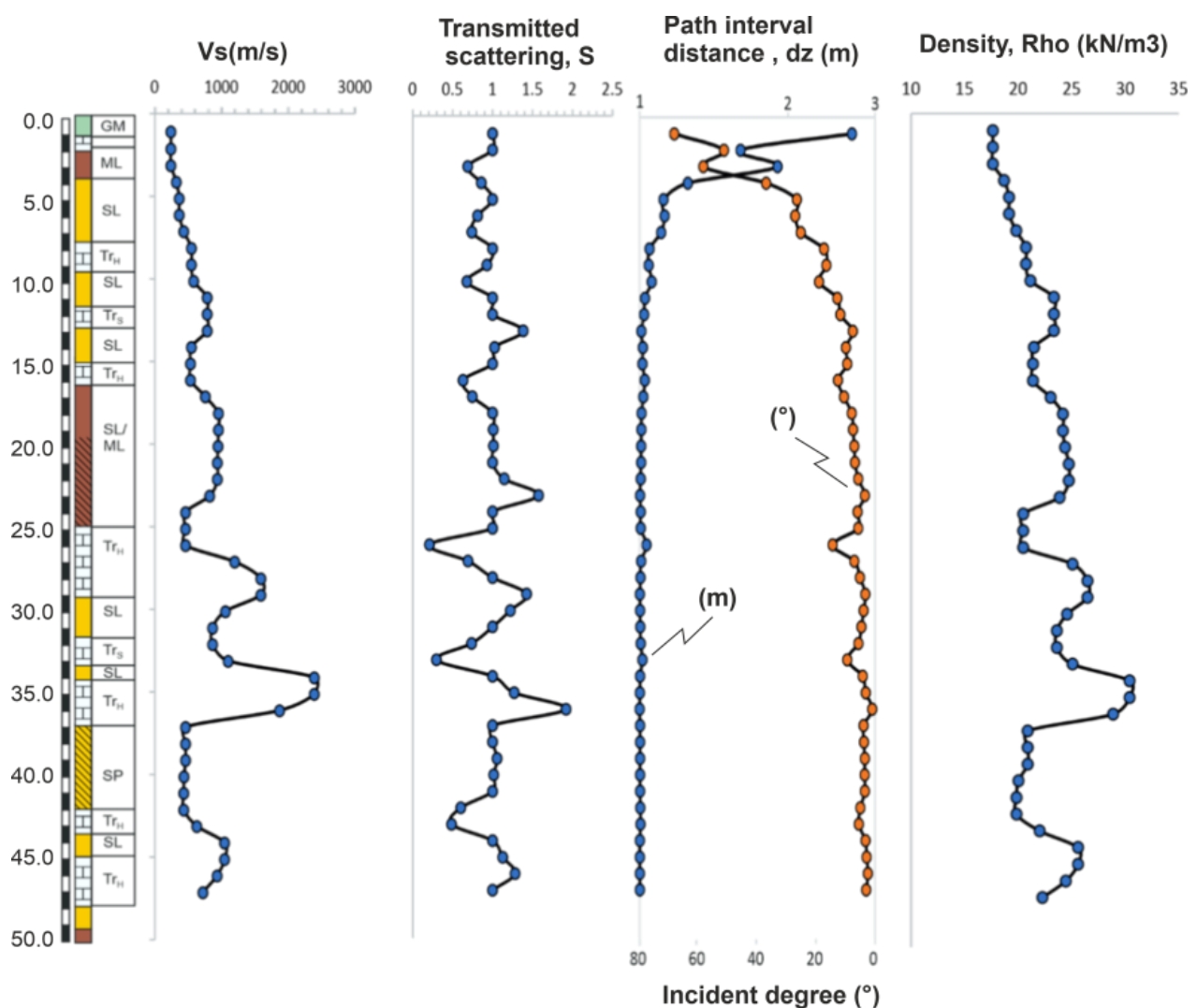


Figure 9. Profiles of variables influencing the SH-wave amplitude.

$$\xi_i = \frac{1}{2\pi f_{c_i} dl_i} \ln \left(\frac{\left| \overline{A^*(z_{i-1})} \right| S_i \sum_1^i dl_i}{\left| \overline{A^*(z_i)} \right| \sum_1^i dl_{(i-1)}} \right) V_{S_i} \quad (19)$$

In this equation, the shear wave velocity, V_{S_i} , derives from the interval velocity profile computed by module 2, and it is used to consider positive and negative signals produced by two opposite hammer shots. In summarizing, for each depth step, each depth set of damping ratio values is composed resolving Equation (19) on a total number of quasi-monochromatic signals given from n from modulated in frequency multiplied by k from wavenumber cut tapering function multiplied by two and given to consider positive and negative polarized signals. Stable outputs result from assuming each set with a number of signals from 30 to 50; in this study, sets composed of 40 signals resulting from $n = 4$, $k = 5$ (Figure 8), for both polarizations, were used.

5.6. Damping Ratio Profile

The previous framework highlights that other phenomena act together with the elastic damping ratio to change the amplitude of signals. Thus, the damping is very difficult to isolate and capture, mainly when its assessment is on short propagation traits. Therefore, in accordance with previous studies, highlighting the difficulty in completely cleaning signals from the alien effects, a stochastic approach is preferred over the deterministic ones, which are most appropriate in controlled laboratory tests. On this basis, the proposed approach assesses the damping ratio value as a trend. This trend is defined in a dataset composed of “trended damping ratio” values, resulting from solving Equation (19) by using signals from Equation (18) in turn. The trend processing necessitates a non-rigorous physical consistency of dataset elements (trended damping ratios) because the magnitude of the assessing variable is comparable with the epistemic error that affects those dataset elements. In this way, the local mathematical drift defines the damping ratio by considering both positive and negative (not physical) trend values. Thus, these values fall in an influence range of -0.20 to 0.20 by excluding other ones. The values of this range, considered in absolute way, are comparable with typical values of elastic damping ratio. This interval is zero-centered, effectively constituting the central Gaussian value of a normal error distribution in the total absence of predominant effects. Therefore, a drift of the trend that is predominant in positive values and moreover consistent with both the nature of ground material and vertical lithological changes suggests that this drift of trend is driven by the damping effect and a good quality estimation is possible (e.g., Figure 10). Shear wave velocity values, defined by the coherent line technique, act on the sensitivity of this model (Equations (12), (14) and (19)) and contribute to defining the number of values composing the metadata-set by the remaining invariant n and k parameters. With this regard, a larger number of values founded for each step highlights good statistical precision, while their short range centered on positive values highlights good statistical accuracy. Good precision and accuracy of the metadata set indicates a greater coherence of scattering assessment and also the adequacy of the V_s profile assumed in the computation. Damping profiles are carried out by data trend combinations that regard both “same-depth” and “near-depth” damping values. Firstly, the median values are obtained from damping values having the same depth. Following this, the moving average of these median values helps to stabilize the damping values along the vertical profile.

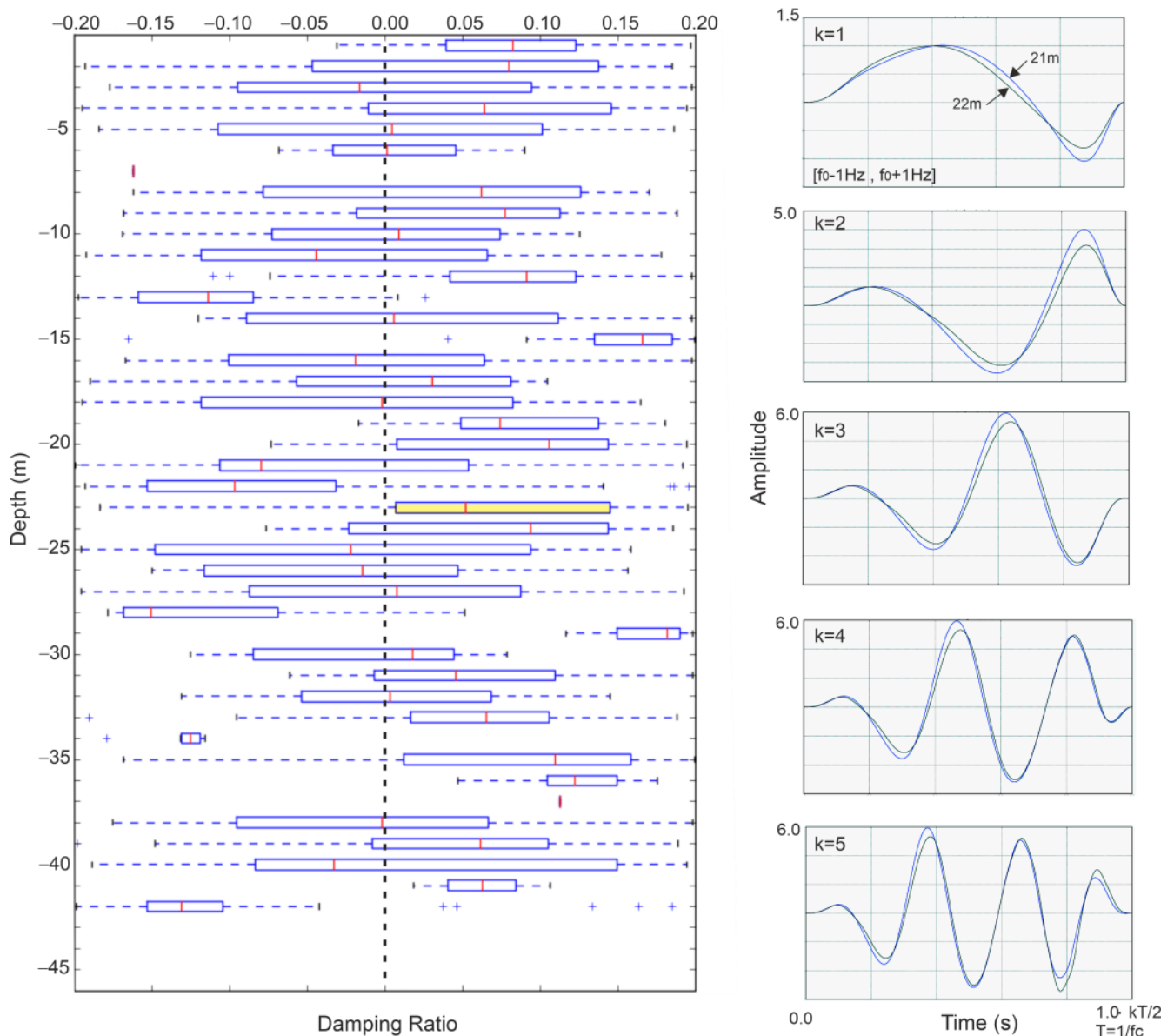


Figure 10. Box plots of damping ratio data trend/distribution with depth and example of wave packet subset regarding the complete wave number set on the first frequency filter interval and on the positive shot in the couple depth 21 and 22 m.

6. Discussion and Validation

In this study, damping profiles result from moving averages computed by considering two and three median values (Figure 11). A buffer reporting the middle tertile (the 33rd to 66th percentiles) marks the dispersion trend too by surrounding the median values along the profile. The damping trend highlights a good affinity with the nature of the lithologies and captures the frequent changes in the complex stratigraphy. This performance is by sensitivity analysis that has suggested a V_s profile from smoothed coherent lines interpolating two progressive depth step values rather than the third and fourth ones. Hard travertine layers widely show negative damping ratio values, while shallow top soils, composed of soft sand and silt deposits, show values within the range of 3.00–5.00%. These loose materials show substantially decreased values in damping and vice versa in increased stiffness (by V_s) when they appear involved by weak travertines process formation, i.e., the sandy material encountered at 5 m and 40 m (very loose) in the borehole b1.

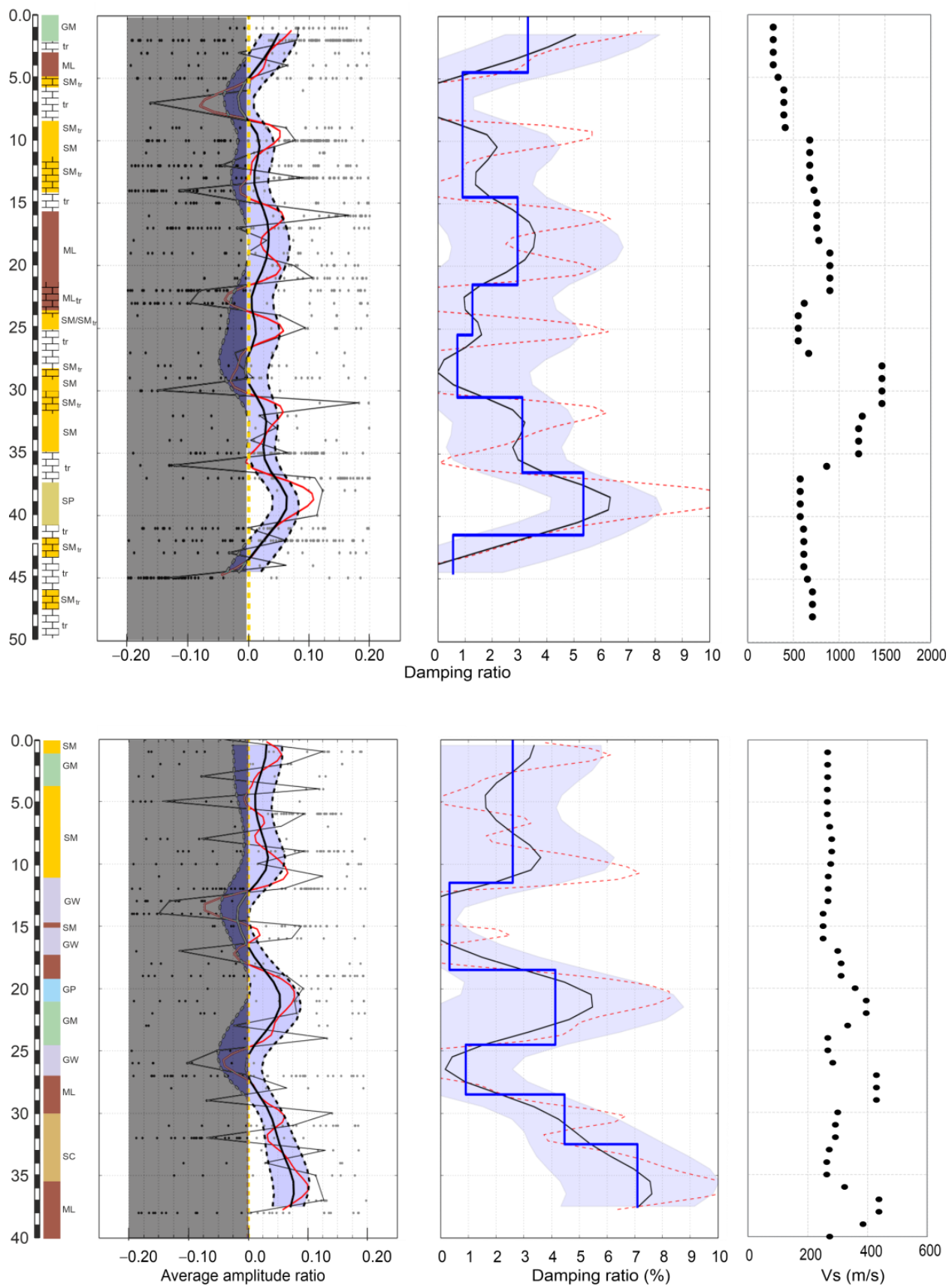


Figure 11. Damping ratio profile computed on Vs interval profiles computed by coherent smoothed line considering interpolation on three z-steps (left) and two z-steps (right).

The damping values measured with this approach are compared with laboratory and in situ measurements detected by other authors (Table 2). The results show downward trends approaching measurements obtained by the laboratory tests for fine material (SM/SC: silty and sandy), for alluvial material (GM/GW: gravel mixed with sand and silt), and close to the in situ results by the third authors for clean sand (SP: clean sand). From this last example, monogranular lithology is defined in a relative way in this study. Data about weak and hard travertine material have not been found in the literature.

Table 2. Comparison with laboratory and in-field measurements.

Material	Laboratory Measurements (%)	Other In Situ Measurements (%)	In Situ Measurement from This Work (%)
GM/GW: gravel mixed to sand and silt	0.5–1.0 [56] 0.5–2.0 [57] 3.0 [58] >30% fine content: 8.0 [59]; <15% fine content: 2.0 [59];	Alluvium 12.0; in [44] by SASW 8.2–10.5 [60];	0.25–4.15
ML: silt and clay	1.5–2.0 [61] 1.0–5.0 [62] 8.0–6.0 [63]	4.0–7.0 [45] 1.7 [64]	3.05–7.02
SM/SC: silty sand	0.8–4.4 [65]	1.7–2.5 [64] 2.5; Kudo and Shima, 1981 in [44]	0.84–4.43
SP: clean sand	1.5 [66] 1.0 [67] 0.5–1.0 in [44]	6.0; Kudo and Shima, 1981 in [31] 4.0; Meissner and Theilen, 1986 in [44]	5.27
TrS: soft travertine or sandy travertine	-	-	<0.00–0.82
TrH: hard travertine	-	-	<0.00

The slope ratio method, which is generally used in combination with the vibrodine device to develop harmonic stationary source signals, is here performed with the previously normalized amplitudes of the source signals (Equation (13)) in order to consider the uncontrolled pulses produced by hammering. The spectral ratio curves are far from the linear uniform trend in a specific frequency interval (border graphs in Figure 10). Therefore, it appears very hard to introduce a robust automatized procedure, such as the frequency-time packets one proposed in this paper. However, the slope ratio method was tried to process a semi-automated procedure to encounter the focus of the work, but mainly for the objectivity in the comparison analysis. This procedure, associated with the slope ratio method is not supported by physical bases. On this premise, the damping values have been defined on a minor gradient intercepted by a linear stationary interval of the spectral ratio curves. This slope is the minor gradient of the linear fit encountered in a short frequency interval of 20 Hz shifting within a bigger interval of 20–100 Hz in the smoothed spectral ratio curve. By applying different moving averages on the spectra ratio curves already previously smoothed by the Konno and Ohmachi function, different smoothed spectra are produced. The best linear fit happens on the moving average of five near values. Finally, the damping depth trend is obtained by a moving average that considers in the computation only damping values in the range of -0.20 to 0.20 . This hiring is the same as used in the frequency-time packets method.

The comparison (Figure 12) shows a common general trend between the two methodologies. Rollovers at 5 m depth, between soft soil and sandy travertine, and at 15 m, between sandy travertine and hard silty sand, are shown for both. Common changes due to the sandy travertine series are also at 25 and 37 m. In general, the values shown by the frequency-time method are often lower than the slope ratio and so a particular decrease in these ones within negative values occurs at the start of the hard travertine series.

Instead, the slope ratio method shows positive values but with scarce reliability, e.g., high damping values in the ranges of 21–25 m and 41–46 m where silty-sandy travertines and hard-travertine appear.

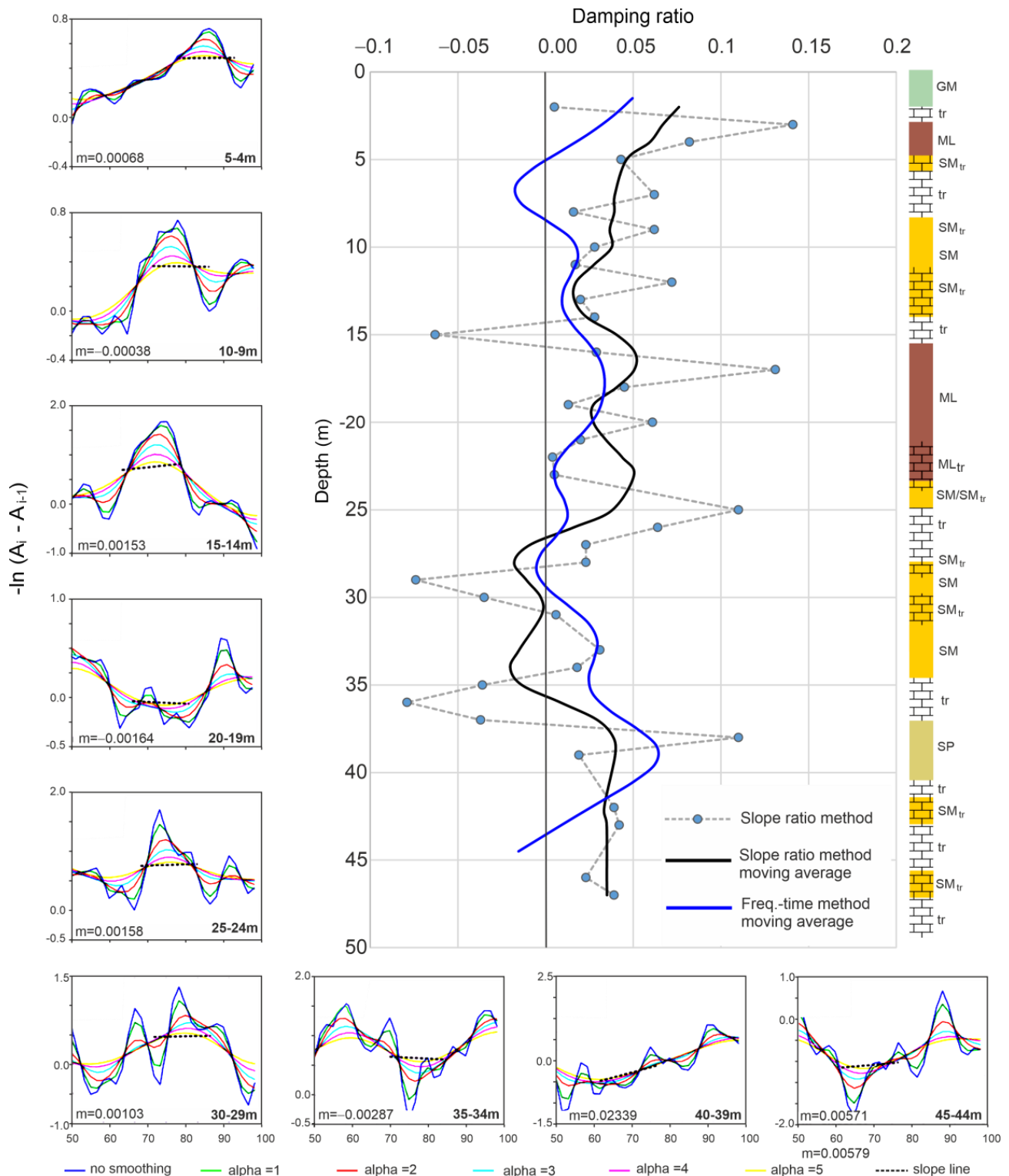


Figure 12. Comparison between the proposed frequency-time method and the slope ratio method. As an example, the border graphs are related to the spectral ratio of the positive pulses in some intervals.

The numerous computational steps at the base of the proposed model encourages the realization of a user-friendly interface to compute all the steps contained in this work. In the current state, Python scripts are organized in computation modules regarding the picking process, velocity profiles, and finally the damping ratio profile development.

7. Conclusions

By considering the specific propensity of the downhole method in the direct measurement of shear wave velocity, the present work aims to implement the accuracy and expand the capability of this method concerning its standard use. This upgrading is to estimate the damping ratio values along the vertical profile, passing to improve the shear wave arrival detection. The method introduces a tapering mask to isolate the direct shear-wave trains from other ones. This function linearly shifts in the series according to an assigned initial delay time and slope. The latter stems from the average of shear wave velocity defined on an unequivocal first arrival intercepted on a depth signal of the series. As shown by the cases dealt with here, the large buffer action of the function permits to preserve all first arrivals from masking even when hard break-slopes are present in the series (high changing of velocity). The wave trains, isolated by the mask tapering function, are the same used in the following damping ratio analysis.

Considering the theoretical propagation path and scattering effects on the wave amplitude, a dedicated algorithm based on a stochastic approach has been introduced, and it constitutes the new model to estimate the damping ratio profile. Different from others, this computerized algorithm does not require substantial integration of the standard equipment, nor does it require step-by-step subjective assumptions during the processing and measures regarding the large depth intervals constituting homogeneous material.

The damping ratio is computed using a frequency-time combined approach on signals corrected from the source effect, geometrical attenuation, and scattering. The damping profiles have been obtained by resolving the amplitude ratios in the time domain of the corrected signals to develop a higher number of packets modulated both in frequency and time. The profile is statistically computed in terms of the local drift of the trend on the amplitude ratio series that would otherwise have a normal distribution centered on zero. The damping profiles obtained using this approach correspond to the lithological changes and are coherent with the field and laboratory and experimental data obtained by other authors with similar materials.

The proposed model can be used for different ground sequences, but its performance is linked to the quality of the signals acquired, and in this regard, users should take into consideration all the suggestions and best practices reported in the introduction of this work and in other ones dealing with this specific topic.

Funding: The open access publication of this paper is thanks to the ReLUIS fund for the study on “Experimentation of guidelines for risk classification and management, safety assessment and monitoring of existing bridges—WP5: site geology and landslide hazard”. Code n. 000330_21_AP__SAPPA. The availability of this fund was granted by Prof. Giuseppe Sappa, to whom my deep gratitude goes. A particular thanks to the Rieti municipal governance and administration for site-access authorizations; reference, Lucia Fortini.

Informed Consent Statement: Informed consent was obtained from all subjects involved in the study.

Data Availability Statement: Code scripts and example data processing are shared on: https://github.com/gerardo-grelle/DH_elaboration (accessed on 5 April 2023).

Acknowledgments: A special thanks is to Francesco De Filippi, Leonardo Maria Giannini, and Valerio De Angelis for the logistic support during the field experimentations.

Conflicts of Interest: The author declares no conflict of interest. The funders had no role in the design of the study; in the collection, analyses, or interpretation of data; in the writing of the manuscript; or in the decision to publish the results.

References

- Uma Maheswari, R.; Boominathan, A.; Dodagoudar, G.R. Development of Empirical Correlation between Shear Wave Velocity and Standard Penetration Resistance in Soils of Chennai City. In Proceedings of the 14th World Conference on Earthquake Engineering (WCEE), Beijing, China, 12–17 October 2008.
- Tan, C.G.; Majid, T.A.; Ariffin, K.S.; Bunnori, N.M. Effects of Site Classification on Empirical Correlation between Shear Wave Velocity and Standard Penetration Resistance for Soils. *Appl. Mech. Mater.* **2013**, 284–287, 1305–1310. [\[CrossRef\]](#)
- Shukla, D.; Solanki, C.H. Estimated Empirical Correlations between Shear Wave Velocity and SPT-N Value for Indore City Using NLR and ANN. *Indian Geotech. J.* **2020**, 50, 784–800. [\[CrossRef\]](#)
- Gautam, D. Empirical Correlation between Uncorrected Standard Penetration Resistance (N) and Shear Wave Velocity (Vs) for Kathmandu Valley, Nepal. *Geomatics. Nat. Hazards Risk* **2017**, 8, 496–508. [\[CrossRef\]](#)
- Kirar, B.; Maheshwari, B.K.; Muley, P. Correlation Between Shear Wave Velocity (Vs) and SPT Resistance (N) for Roorkee Region. *Int. J. Geosynth. Ground Eng.* **2016**, 2, 1–11. [\[CrossRef\]](#)
- Strelec, S.; Stanko, D.; Gazdek, M. Empirical Correlation between the Shear-Wave Velocity and the Dynamic Probing Heavy Test: Case Study, Varaždin, Croatia. *Acta Geotech. Slov.* **2016**, 13, 3–15.
- Hussien, M.N.; Karray, M. Shear wave velocity as a geotechnical parameter: An overview. *Can. Geotech. J.* **2016**, 53, 252–272. [\[CrossRef\]](#)
- Long, M.; Donohue, S. Characterization of Norwegian marine clays with combined shear wave velocity and piezocone cone penetration test (CPTU) data. *Can. Geotech. J.* **2010**, 47, 709–718. [\[CrossRef\]](#)
- L'heureux, J.-S.; Long, M. Relationship between Shear-Wave Velocity and Geotechnical Parameters for Norwegian Clays. *J. Geotech. Geoenviron. Eng.* **2017**, 143, 04017013. [\[CrossRef\]](#)
- Ku, T.; Mayne, P.W. In Situ Lateral Stress Coefficient (K0) from Shear Wave Velocity Measurements in Soils. *J. Geotech. Geoenviron. Eng.* **2015**, 141, 06015009. [\[CrossRef\]](#)
- Duan, W.; Cai, G.; Liu, S.; Puppala, A.J. Correlations between Shear Wave Velocity and Geotechnical Parameters for Jiangsu Clays of China. *Pure Appl. Geophys.* **2019**, 176, 669–684. [\[CrossRef\]](#)
- Ayres, A.; Theilen, F. Relationship between P- and S-wave velocities and geological properties of near-surface sediments of the continental slope of the Barents Sea. *Geophys. Prospect.* **1999**, 47, 431–441. [\[CrossRef\]](#)
- Fratta, D.; Santamarina, J.C. Shear wave propagation in jointed rock: State of stress. *Géotechnique* **2002**, 52, 495–505. [\[CrossRef\]](#)
- Greenberg, M.L.; Castagna, J.P. Shear-wave velocity estimation in porous rocks: Theoretical formulation, preliminary verification and applications1. *Geophys. Prospect.* **1992**, 40, 195–209. [\[CrossRef\]](#)
- Zhang, L. A simple method for evaluating liquefaction potential from shear wave velocity. *Front. Arch. Civ. Eng. China* **2010**, 4, 178–195. [\[CrossRef\]](#)
- Youd, T.L.; Idriss, I.M. Liquefaction Resistance of Soils: Summary Report from the 1996 NCEER and 1998 NCEER/NSF Workshops on Evaluation of Liquefaction Resistance of Soils. *J. Geotech. Geoenviron. Eng.* **2001**, 127, 297–313. [\[CrossRef\]](#)
- Tokimatsu, K.; Uchida, A. Correlation Between Liquefaction Resistance and Shear Wave Velocity. *Soils Found.* **1990**, 30, 33–42. [\[CrossRef\]](#)
- Lin, P.-S.; Chang, C.-W.; Chang, W.-J. Characterization of liquefaction resistance in gravelly soil: Large hammer penetration test and shear wave velocity approach. *Soil Dyn. Earthq. Eng.* **2004**, 24, 675–687. [\[CrossRef\]](#)
- Kayabali, K. Soil liquefaction evaluation using shear wave velocity. *Eng. Geol.* **1996**, 44, 121–127. [\[CrossRef\]](#)
- Qiu, T.; Huang, Y.; Guadalupe-Torres, Y.; Baxter, C.D.P.; Fox, P.J. Effective Soil Density for Small-Strain Shear Waves in Saturated Granular Materials. *J. Geotech. Geoenviron. Eng.* **2015**, 141, 04015036. [\[CrossRef\]](#)
- Andrus, R.D.; Stokoe, K.H.; Juang, C.H. Guide for Shear-Wave-Based Liquefaction Potential Evaluation. *Earthq. Spectra* **2004**, 20, 285–308. [\[CrossRef\]](#)
- Andrus, R.D.; Ii, K.H.S. Liquefaction Resistance of Soils from Shear-Wave Velocity. *J. Geotech. Geoenviron. Eng.* **2000**, 126, 1015–1025. [\[CrossRef\]](#)
- Amoly, R.S.; Ishihara, K.; Bilsel, H. The relation between liquefaction resistance and shear wave velocity for new and old deposits. *Soils Found.* **2016**, 56, 506–519. [\[CrossRef\]](#)
- Grelle, G.; Guadagno, F.M. Seismic refraction methodology for groundwater level determination: “Water seismic index”. *J. Appl. Geophys.* **2009**, 68, 301–320. [\[CrossRef\]](#)
- Hamada, G.M. Reservoir Fluids Identification Using Vp/Vs Ratio? *Oil Gas Sci. Technol.* **2004**, 59, 649–654. [\[CrossRef\]](#)
- Bourdeau, C.; Lenti, L.; Cercato, M.; Hailemichael, S.; Martino, S.; Varone, C. Numerical Modelling of Local Seismic Response in Alluvial Valleys Filled by Heterogeneous Deposits for Seismic Microzonation Studies in Northern Latium (Italy). In *Earthquake Geotechnical Engineering for Protection and Development of Environment and Constructions*; CRC Press: Boca Raton, FL, USA, 2019.
- Cercato, M.; De Donno, G.; Di Giulio, A.; Lanzo, G.; Tommasi, P. Dynamic characterization of the hill of Civita di Bagnoregio (Viterbo, Central Italy) for seismic response analysis. *Eng. Geol.* **2019**, 266, 105463. [\[CrossRef\]](#)
- Grelle, G.; Gargini, E.; Facciorusso, J.; Maresca, R.; Madii, C. Seismic site effects in the Red Zone of Amatrice hill detected via the mutual sustainment of experimental and computational approaches. *Bull. Earthq. Eng.* **2020**, 18, 1955–1984. [\[CrossRef\]](#)
- Grelle, G.; Bonito, L.; Rosalba, M.; Iacurto, S.; Madii, C.; Revellino, P.; Sappa, G. Topographic effects observed at Amatrice hill during the 2016–2017 Central Italy seismic sequence. *Earthq. Eng. Eng. Vib.* **2021**, 20, 63–78. [\[CrossRef\]](#)

30. Luo, Y.-H.; Xu, Q.; Zhan, W.-W.; Grelle, G. Seismic hazard prediction using multispectral amplification maps in a complex topographic area: A case study of Qiaozhuang town, Sichuan Province, Southwest China. *J. Mt. Sci.* **2022**, *19*, 726–739. [\[CrossRef\]](#)
31. Grelle, G.; Guadagno, F.M. Regression analysis for seismic slope instability based on a double phase viscoplastic sliding model of the rigid block. *Landslides* **2013**, *10*, 583–597. [\[CrossRef\]](#)
32. Grelle, G.; Sappa, G.; Madiati, C. SHAKER: A selector of consistent and energetically equalized natural ground motions using the Italian earthquake database. *Eng. Geol.* **2023**, *316*, 107046. [\[CrossRef\]](#)
33. Xia, J.; Miller, R.D.; Park, C.B.; Hunter, J.A.; Harris, J.B. Comparing Shear-Wave Velocity Profiles from MASW with Borehole Measurements in Unconsolidated Sediments, Fraser River Delta, B.C., Canada. *J. Environ. Eng. Geophys.* **2000**, *5*, 1–13. [\[CrossRef\]](#)
34. Lebedev, M.; Dorokhin, K. Application of Cross-Hole Tomography for Assessment of Soil Stabilization by Grout Injection. *Geosciences* **2019**, *9*, 399. [\[CrossRef\]](#)
35. Rao, Y.; Wang, Y. Crosshole seismic tomography: Working solutions to issues in real data travel time inversion. *J. Geophys. Eng.* **2005**, *2*, 139–146. [\[CrossRef\]](#)
36. Beeston, H.E.; McEvilly, T.V. Shear wave velocities from down-hole measurements. *Earthq. Eng. Struct. Dyn.* **1977**, *5*, 181–190. [\[CrossRef\]](#)
37. Meredith, J.A.; Toksoz, M.N.; Cheng, C.H. Secondary shear waves from source boreholes1. *Geophys. Prospect.* **1993**, *41*, 287–312. [\[CrossRef\]](#)
38. Crice, D. Near-surface, downhole shear-wave surveys: A primer. *Geophysics* **2011**, *30*, 164–171. [\[CrossRef\]](#)
39. Maheshwari, B.K.; Kirar, B. Dynamic properties of soils at low strains in Roorkee region using resonant column tests. *Int. J. Geotech. Eng.* **2017**, *13*, 399–410. [\[CrossRef\]](#)
40. Ciancimino, A.; Lanzo, G.; Alleanza, G.A.; Amoroso, S.; Bardotti, R.; Biondi, G.; Cascone, E.; Castelli, F.; Di Giulio, A.; D'onofrio, A.; et al. Dynamic characterization of fine-grained soils in Central Italy by laboratory testing. *Bull. Earthq. Eng.* **2019**, *18*, 5503–5531. [\[CrossRef\]](#)
41. Molina-Gómez, F.; da Fonseca, A.V.; Ferreira, C.; Camacho-Tauta, J. Dynamic properties of two historically liquefiable sands in the Lisbon area. *Soil Dyn. Earthq. Eng.* **2020**, *132*, 106101. [\[CrossRef\]](#)
42. Crow, H.; Hunter, J.; Motazedian, D. Monofrequency in situ damping measurements in Ottawa area soft soils. *Soil Dyn. Earthq. Eng.* **2011**, *31*, 1669–1677. [\[CrossRef\]](#)
43. Jamiolkowski, M.; LoPresti, D.; Pallara, O. Role of In-Situ Testing in Geotechnical Earthquake Engineering. In Proceedings of the International Conferences on Recent Advances in Geotechnical Earthquake Engineering and Soil Dynamics, St. Louis, MO, USA, 2–7 April 1995.
44. Stewart, W.P.; Campanella, R.G. Practical aspects of in situ measurements of material damping with the seismic cone penetration test. *Can. Geotech. J.* **1993**, *30*, 211–219. [\[CrossRef\]](#)
45. Mok, Y.J.; Sanchez-Salinerio, I.; Stokoe, K.H.; Roesset, J.M. In Situ Damping Measurements by Crosshole Seismic Method. In *Earthquake Engineering and Soil Dynamics II—Recent Advances in Ground-Motion Evaluation*; Geotechnical Special Publication 20; ASCE: New York, NY, USA, 1988; pp. 305–320.
46. Hardin, B.O.; Drnevich, V.P. Shear Modulus and Damping in Soils: Design Equations and Curves. *J. Soil Mech. Found. Div.* **1972**, *98*, 667–692. [\[CrossRef\]](#)
47. Huang, X.; Zhou, A.; Wang, W.; Jiang, P. Characterization of the Dynamic Properties of Clay–Gravel Mixtures at Low Strain Level. *Sustainability* **2020**, *12*, 1616. [\[CrossRef\]](#)
48. Park, D.; Kishida, T. Shear modulus reduction and damping ratio curves for earth core materials of dams. *Can. Geotech. J.* **2019**, *56*, 14–22. [\[CrossRef\]](#)
49. Chong, S.-H. Soil Dynamic Constitutive Model for Characterizing the Nonlinear-Hysteretic Response. *Appl. Sci.* **2017**, *7*, 1110. [\[CrossRef\]](#)
50. Soból, E.; Głuchowski, A.; Szymański, A.; Sas, W. The New Empirical Equation Describing Damping Phenomenon in Dynamically Loaded Subgrade Cohesive Soils. *Appl. Sci.* **2019**, *9*, 4518. [\[CrossRef\]](#)
51. Zhang, J.; Andrus, R.D.; Juang, C.H. Normalized Shear Modulus and Material Damping Ratio Relationships. *J. Geotech. Geoenviron. Eng.* **2005**, *131*, 453–464. [\[CrossRef\]](#)
52. Chehat, A.; Harichane, Z.; Karray, M. Non-linear soil modelling by correction of the hysteretic damping using a modified Iwan model together with Masing rules. *Int. J. Geotech. Eng.* **2017**, *13*, 581–593. [\[CrossRef\]](#)
53. Keçeli, A. Soil Parameters Which Can Be Determined with Seismic Velocities. *Jeofizik* **2012**, *16*, 17–29.
54. Grelle, G.; Bonito, L.; Lampasi, A.; Revellino, P.; Guerriero, L.; Sappa, G.; Guadagno, F.M. SiSeRHMap v1.0: A simulator for mapped seismic response using a hybrid model. *Geosci. Model Dev.* **2016**, *9*, 1567–1596. [\[CrossRef\]](#)
55. Konno, K.; Ohmachi, T. A smoothing function suitable for estimation of amplification factor of the surface ground from microtremor and its application. *Doboku Gakkai Ronbunshu* **1995**, *1995*, 247–259. [\[CrossRef\]](#) [\[PubMed\]](#)
56. Bayat, M.; Ghalandarzadeh, A. Stiffness Degradation and Damping Ratio of Sand-Gravel Mixtures Under Saturated State. *Int. J. Civ. Eng.* **2018**, *16*, 1261–1277. [\[CrossRef\]](#)
57. Seed, H.B.; Wong, R.T.; Idriss, I.M.; Tokimatsu, K. Moduli and Damping Factors for Dynamic Analyses of Cohesionless Soils. *J. Geotech. Eng.* **1986**, *112*, 1016–1032. [\[CrossRef\]](#)
58. Lin, S.-Y.; Lin, P.S.; Luo, H.-S.; Juang, C.H. Shear modulus and damping ratio characteristics of gravelly deposits. *Can. Geotech. J.* **2000**, *37*, 638–651. [\[CrossRef\]](#)

59. Aghaei Araei, A.; Soroush, A.; Rayhani, M. Large-Scale Triaxial Testing and Numerical Modeling of Rounded and Angular Rockfill Materials. *Sci. Iran.* **2010**, *17*, 169–183.
60. Bawadi, N.F.; Nayan, K.A.M.; Taha, M.R.; Omar, N.A. Estimate of Small Stiffness and Damping Ratio in Residual Soil Using Spectral Analysis of Surface Wave Method. *MATEC Web Conf.* **2016**, *47*, 03017. [[CrossRef](#)]
61. Zavoral, D. Dynamic Properties of an Undisturbed Clay from Resonant Column Tests. Ph.D. Thesis, University of British Columbia, Vancouver, BC, Canada, 1990. [[CrossRef](#)]
62. Sun, J.I.; Golesorkhi, R.; Seed, H.B. *Dynamic Moduli and Damping Ratios for Cohesive Soils*; Earthquake Engineering Research Center—Report No. UCB/EERC-88/11; College of Engineering, University of California at Berkeley: Berkeley, CA, USA, 1988.
63. Xenaki, V.; Athanasopoulos, G. Liquefaction resistance of sand–silt mixtures: An experimental investigation of the effect of fines. *Soil Dyn. Earthq. Eng.* **2003**, *23*, 1–12. [[CrossRef](#)]
64. Tonouchi, K.; Sakayama, T.; Imai, T. S wave velocity in the ground and the damping factor. *Bull. Int. Assoc. Eng. Geol. Bull. L'association Int. Géol. L'ingénieur* **1982**, *26*, 327–333.
65. Senetakis, K.; He, H. Dynamic characterization of a biogenic sand with a resonant column of fixed–partly fixed boundary conditions. *Soil Dyn. Earthq. Eng.* **2017**, *95*, 180–187. [[CrossRef](#)]
66. Ishihara, K. Chapter—Evaluation of soil properties for use in earthquake response analysis. In *Geomechanical Modelling in Engineering Practice*; Dungar, R., Studer, J.A., Eds.; Routledge: London, UK, 1986; pp. 241–275. ISBN 9780203753583. [[CrossRef](#)]
67. Saxena, S.K.; Reddy, K.R. Dynamic Moduli and Damping Ratios for Monterey No. 0 Sand by Resonant Column Tests. *Soils Found.* **1989**, *29*, 37–51. [[CrossRef](#)]

Disclaimer/Publisher's Note: The statements, opinions and data contained in all publications are solely those of the individual author(s) and contributor(s) and not of MDPI and/or the editor(s). MDPI and/or the editor(s) disclaim responsibility for any injury to people or property resulting from any ideas, methods, instructions or products referred to in the content.